nature nanotechnology

SUPPLEMENTARY INFORMATION

DOI: 10.1038/NNANO.2013.145

Symmetry and magnitude of spin-orbit torques in ferromagnetic heterostructures

Kevin Garello, Ioan Mihai Miron, Can Onur Avci, Frank Freimuth,
Yuriy Mokrousov, Stefan Blügel, Stéphane Auffret, Olivier Boulle,
Gilles Gaudin, and Pietro Gambardella

Table of Contents:

S1. General expression for the spin accumulation and SOTs

In this section we derive general expressions for the spin accumulation ($\delta\boldsymbol{m}$), effective fields ($\boldsymbol{B}^I$), and torques ($\boldsymbol{T}$) induced by an electric current in trilayers with structure inversion asymmetry along the stacking direction *z*. The current is driven by an applied electric field ($\boldsymbol{E}$) in the *xy* plane. We consider only the case of trilayers that exhibit continuous rotational symmetry about the *z* axis and mirror symmetry for all the planes that are perpendicular to the *xy* plane, i.e., contain the *z* axis. The results of this section apply to samples that are either polycrystalline, as in our case, or disordered. In fully epitaxial systems that display discrete rotational symmetry around the stacking direction it is expected also that $\delta\boldsymbol{m}$, $\boldsymbol{B}^I$, and $\boldsymbol{T}$ vary as the sample is rotated while keeping the directions of the electric field and magnetization fixed in space.

Consider an applied current that leads to a spin accumulation $\delta\boldsymbol{m}$. Explicitly, in the equations below, $\delta\boldsymbol{m}$ denotes the induced magnetization associated with the spin accumulation. $\delta\boldsymbol{m}$ induces a change of the exchange field ($\delta\boldsymbol{B}^{xc}$) in the ferromagnet, which acts as an effective magnetic field on the magnetization ($\boldsymbol{m}$), given by $\boldsymbol{B}^I = \delta\boldsymbol{B}^{xc} = \frac{B^{xc}}{m}\delta\boldsymbol{m}$. The resulting torque is given by $\boldsymbol{T} = \boldsymbol{m} \times \boldsymbol{B}^I$. Since the torque depends only on the component of $\boldsymbol{B}^I$ that is perpendicular to $\boldsymbol{m}$, in the following $\boldsymbol{B}^I$ and $\delta\boldsymbol{m}$ will denote the perpendicular components of the effective field and the spin accumulation, respectively.

In Fig. S1a and b we consider the case of magnetization in the *xz* plane and electric field in the *x* direction. We show that symmetry allows for two components for the spin accumulation: A longitudinal one, $\delta\boldsymbol{m}^{\parallel}$, which lies in the *xz* plane, and a perpendicular one, $\delta\boldsymbol{m}^{\perp}$, which points in the *y* direction. $\boldsymbol{E}$ is invariant under mirror reflection at the *xz* plane. However, $\boldsymbol{m}$ is inverted, because it is an axial vector. Similarly, the component $\delta\boldsymbol{m}^{\parallel}$ of the axial vector $\delta\boldsymbol{m}$ is inverted, but $\delta\boldsymbol{m}^{\perp}$ is invariant. Thus, $\delta\boldsymbol{m}^{\parallel}$ has to be an odd function of $\boldsymbol{m}$, while $\delta\boldsymbol{m}^{\perp}$ has to be an even function. Mirror reflection at the *yz* plane followed by a rotation around the *z* axis by 180° leads to the same conclusion. There is no symmetry operation that forbids either $\delta\boldsymbol{m}^{\parallel}$ or $\delta\boldsymbol{m}^{\perp}$, owing to the structure inversion asymmetry. For example, if there was inversion symmetry, $\boldsymbol{E}$ would change under inversion while $\boldsymbol{m}$ and $\delta\boldsymbol{m}$ would remain unchanged. Thus, inversion symmetry would dictate that both $\boldsymbol{E}$ and $-\boldsymbol{E}$ lead to the same spin accumulation, meaning that, in such a case, the linear response of the spin accumulation would have to be zero.

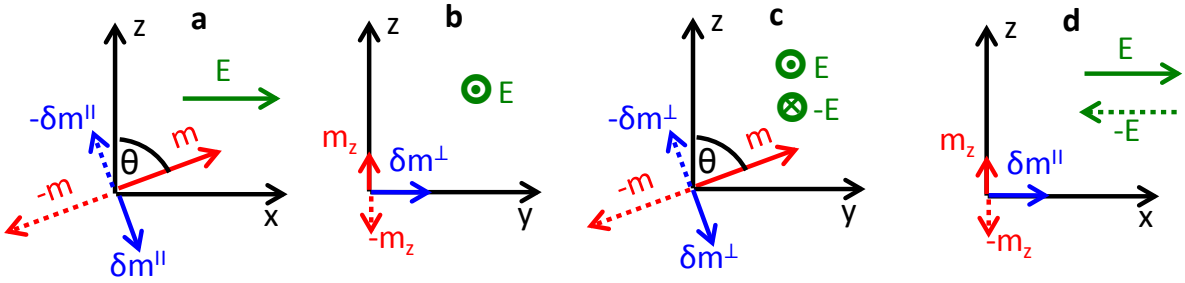

Figure S1. Transformation of electric field $\boldsymbol{E}$, magnetization $\boldsymbol{m}$ and spin accumulation $\delta\boldsymbol{m}$ under mirror reflections. a) Magnetization in the *xz* plane. Mirror reflection at the *xz* plane leaves $\boldsymbol{E}$ invariant, but inverts $\boldsymbol{m}$ and $\delta\boldsymbol{m}^{\parallel}$, because the latter two transform like axial vectors. b) Same as a, but view on the *yz* plane. $\delta\boldsymbol{m}^{\perp}$ is invariant under reflection at the *xz* plane. c) Magnetization in the *yz* plane. Mirror reflection at the *yz* plane inverts $\boldsymbol{E}$, $\boldsymbol{m}$ and $\delta\boldsymbol{m}^{\perp}$. d) Same as c, but view on the *xz* plane. The component $\delta\boldsymbol{m}^{\parallel}$ is invariant under reflection at the *yz* plane.

In Fig. S1c and d we consider the case of magnetization in the *yz* plane and the electric field again along the *x* direction. The longitudinal spin accumulation, $\delta\boldsymbol{m}^{\parallel}$, points now in the *x* direction, while the transverse spin accumulation, $\delta\boldsymbol{m}^{\perp}$, lies in the *yz* plane. Mirror reflection at the *yz* plane inverts $\boldsymbol{E}$, $\boldsymbol{m}$, and $\delta\boldsymbol{m}^{\perp}$, while $\delta\boldsymbol{m}^{\parallel}$ is invariant. Within linear response, $\delta\boldsymbol{m}$ must change sign upon inversion of $\boldsymbol{E}$. It follows that $\delta\boldsymbol{m}^{\perp}$ is again an even function of $\boldsymbol{m}$ because, for inverted electric field and inverted magnetization, $\delta\boldsymbol{m}^{\perp}$ is inverted. Likewise, $\delta\boldsymbol{m}^{\parallel}$ is again an odd function of $\boldsymbol{m}$. Mirror reflection at the *xz* plane followed by a rotation around the *z* axis by 180° leads to the same conclusion. In the special case of $\boldsymbol{m} \parallel y$, $\delta\boldsymbol{m}$ vanishes because in this case mirror reflection at the *yz* plane followed by a rotation around *z* by 180° leaves $\boldsymbol{m}$ and $\boldsymbol{E}$ invariant, but $\delta\boldsymbol{m}$ is inverted. However, if $\boldsymbol{m}$ has nonzero out-of-plane components, there is no symmetry operation present which forbids any of the two components $\delta\boldsymbol{m}^{\parallel}$ or $\delta\boldsymbol{m}^{\perp}$. We will show below that, for $\boldsymbol{m}$ lying in the *xz* plane, one has

$$\delta\boldsymbol{m}^{\parallel} = \frac{E}{B^{xc}}(\boldsymbol{e}_y \times \boldsymbol{m})\left(A_0^{\varphi} + A_2^{\varphi}\sin^2\theta + A_4^{\varphi}\sin^4\theta + \cdots\right) \qquad (1)$$

and

$$\delta\boldsymbol{m}^{\perp} = -\frac{E}{B^{xc}}\boldsymbol{e}_y\left(A_0^{\theta} + A_2^{\theta}\sin^2\theta + A_4^{\theta}\sin^4\theta + \cdots\right) \qquad (2)$$

For $\boldsymbol{m}$ lying in the *yz* plane one has instead:

$$\delta\boldsymbol{m}^{\parallel} = \frac{E}{B^{xc}}(\boldsymbol{e}_y \times \boldsymbol{m})\left(A_0^{\varphi} + B_2^{\theta}\sin^2\theta + B_4^{\theta}\sin^4\theta + \cdots\right) \qquad (3)$$

and

$$\delta\boldsymbol{m}^{\perp} = -\frac{E}{B^{xc}}(\boldsymbol{e}_y \times \boldsymbol{m}) \times \boldsymbol{m}\left(A_0^{\theta} - B_2^{\varphi}\sin^2\theta - B_4^{\varphi}\sin^4\theta - \cdots\right). \qquad (4)$$

The coefficients $A_2^\varphi, A_4^\varphi, A_2^\theta, A_4^\theta$ and $B_2^\varphi, B_4^\varphi, B_2^\theta, B_4^\theta$ describe what we refer to as anisotropy of the SOT. In the absence of anisotropy, one single parameter, A_0^φ, governs the longitudinal accumulation $\delta\boldsymbol{m}^\parallel$, whereas one single parameter, A_0^θ, governs the transverse accumulation $\delta\boldsymbol{m}^\perp$. To describe the anisotropy one needs four parameters for each order of the expansion, where two A parameters describe the anisotropy of the two spin-accumulation components for the case of magnetization in the *xz* plane and two B parameters describe the anisotropy for the case of magnetization in the *yz* plane. Since the trilayers considered in this work exhibit continuous rotational symmetry around the *z* axis, no additional anisotropy arises from the angle φ of the magnetization.

Whereas symmetry arguments provide general expressions of $\delta\boldsymbol{m}^\parallel$ and $\delta\boldsymbol{m}^\perp$, as will be shown below, the same arguments do not provide information about the magnitude of these two terms and the underlying mechanisms. Experiment and theory suggest that both components can be important, and their origin is a matter of debate. As the angle θ in Fig. S1 is varied, the magnitudes of $\delta\boldsymbol{m}^\parallel$ and $\delta\boldsymbol{m}^\perp$ are generally expected to change. The resulting anisotropy in the spin accumulation can arise from spin-dependent interface resistances that influence the spin current from the spin Hall effect as it traverses the interface, or from anisotropic relaxation times, as pointed out in Ref. 1. From the electronic structure point of view, the band energies and thus also the Fermi surface change as a function of θ due to spin-orbit coupling. This can be understood, e.g., in an *sd* model, where only the *s* electrons are subject to Rashba type spin orbit interaction: In the absence of hybridization the spin of the *s*-bands is determined by the Rashba interaction, while the spin of the *d*-bands is determined by the direction of the exchange field. Due to hybridization, the coupled *sd* model exhibits a band structure which depends on θ. The symmetries of the trilayers restrict the allowed θ dependence.

In order to obtain an expression for the spin accumulation valid for any orientation of $\boldsymbol{m}$, one can decompose the electric field into two components, one parallel to the plane spanned by $\boldsymbol{m}$ and the *z* axis (Eqs. 1 and 2) and one perpendicular to it (Eqs. 3 and 4). Since we are considering the linear response of the spin accumulation to an electric field, $\delta\boldsymbol{m}$ is given by a superposition of these two simple cases in general. In the following, we work out a general expression for the linear response of axial vectors (such as $\delta\boldsymbol{m}$, $\boldsymbol{B}^I$, and $\boldsymbol{T}$) to an applied electric field which conforms with the symmetry requirements discussed above. The following derivation holds for all axial vectors perpendicular to the magnetization; however, to be concrete, we refer to torque $\boldsymbol{T}$ and torkance $\boldsymbol{t}$. Readers who are more familiar with spin

accumulation may consider $\boldsymbol{T}$ as spin-accumulation and $\boldsymbol{t}$ as spin-accumulation per applied electric field.

If the electric field is along the x axis, the torque acting on the magnetization can be written as $\boldsymbol{T}(\theta,\varphi) = \boldsymbol{t}(\theta,\varphi)E$, where $\boldsymbol{t}(\theta,\varphi)$ is the torkance and (θ,φ) are the polar and azimuthal coordinates of the unit magnetization vector $\boldsymbol{m} = (\sin\theta\cos\varphi, \sin\theta\sin\varphi, \cos\theta)$. Since the torkance is perpendicular to the magnetization, it may be expressed in terms of the basis vectors of the spherical coordinate system $\boldsymbol{e}_\theta = (\cos\theta\cos\varphi, \cos\theta\sin\varphi, -\sin\theta)$ and $\boldsymbol{e}_\varphi = (-\sin\varphi, \cos\varphi, 0)$ with components $t_\theta(\theta,\varphi)$ and $t_\varphi(\theta,\varphi)$:

$$\boldsymbol{t}(\theta,\varphi) = t_\theta(\theta,\varphi)\boldsymbol{e}_\theta + t_\varphi(\theta,\varphi)\,\boldsymbol{e}_\varphi = \sum_{s=\theta,\varphi} t_s(\theta,\varphi)\boldsymbol{e}_s \ . \qquad (5)$$

It is assumed that the magnetic layer exhibits continuous rotational symmetry around the z axis and mirror symmetry with respect to planes perpendicular to the layer plane. We consider first the consequences of rotational symmetry. If the electric field makes an angle γ with the x axis (Fig. S2a), we have $\boldsymbol{E} = (\cos\gamma, \sin\gamma, 0)E$ and the torque can be rewritten as $\boldsymbol{T}(\theta,\varphi) = \sum_{s=\theta,\varphi} t_s(\theta,\varphi-\gamma)E\boldsymbol{e}_s$. Since the torque is linear in the electric field, we can decompose $\boldsymbol{T}(\theta,\varphi)$ into one component due to the electric field $E\cos\gamma$ along the x direction plus a second component due to the electric field $E\sin\gamma$ along the y direction: $\boldsymbol{T}(\theta,\varphi) = \sum_{s=\theta,\varphi} t_s(\theta,\varphi)E\cos\gamma\,\boldsymbol{e}_s + \sum_{s=\theta,\varphi} t_s(\theta,\varphi-\pi/2)E\sin\gamma\,\boldsymbol{e}_s$. The continuous rotation axis thus leads to the condition $t_s(\theta,\varphi-\gamma) = t_s(\theta,\varphi)\cos\gamma + t_s(\theta,\varphi-\pi/2)\sin\gamma$, which restricts the allowed φ-dependence such that

$$t_s(\theta,\varphi) = F_1^s(\theta)\cos\varphi + F_2^s(\theta)\sin\varphi, \qquad (6)$$

where F_1^s and F_2^s are two functions of θ.

As the magnetization and torque are axial vectors, the x and z components change sign under mirror reflection with respect to the xz plane, while the y component is conserved (Fig. S2b). Mirror reflection symmetry thus dictates that $t_x(\pi-\theta,\pi-\varphi) = -t_x(\theta,\varphi)$, $t_y(\pi-\theta,\pi-\varphi) = t_y(\theta,\varphi)$ and $t_z(\pi-\theta,\pi-\varphi) = -t_z(\theta,\varphi)$, which is equivalent to

$$t_s(\pi-\theta,\pi-\varphi) = -t_s(\theta,\varphi)\ . \qquad (7)$$

Mirror reflection with respect to the yz plane changes the sign of the y and z components of the magnetization and torkance as well as the sign of the electric field along the x direction (Fig. S2c), leading to the conditions $t_x(\pi-\theta,-\varphi) = -t_x(\theta,\varphi)$, $t_y(\pi-\theta,-\varphi) = t_y(\theta,\varphi)$ and $t_z(\pi-\theta,-\varphi) = t_z(\theta,\varphi)$, or, equivalently, to

$$t_s(\pi-\theta,-\varphi)=t_s(\theta,\varphi)\ . \tag{8}$$

Since the angles $(-\theta,\varphi)$ and $(\theta,\pi+\varphi)$ are equivalent, an additional condition is given by

$$t_s(-\theta,\varphi)=-t_s(\theta,\pi+\varphi)\ , \tag{9}$$

where the minus sign on the right hand side compensates for the minus sign on the right hand side in $\boldsymbol{e}_s(-\theta,\varphi)=-\boldsymbol{e}_s(\theta,\pi+\varphi)$.

We expand the functions F_j^s in Eq. 6 as a Fourier series,

$$F_j^s(\theta)=A_{j,0}^s+\sum_{n=1}^{\infty}\left(A_{j,n}^s\cos n\theta+B_{j,n}^s\sin n\theta\right)\ , \tag{10}$$

and note that Eq. 9 is satisfied if $F_j^s(-\theta)=F_j^s(\theta)$, and Eq. 7 as well as Eq. 8 are satisfied if $F_1^s(\pi-\theta)=F_1^s(\theta)$ and $F_2^s(\pi-\theta)=-F_2^s(\theta)$. The condition $F_j^s(-\theta)=F_j^s(\theta)$ rules out terms proportional to $\sin n\theta$ in the Fourier expansion of $F_j^s(\theta)$. Additionally, $\cos n\theta$ terms with odd integers n are ruled out in the expansion of F_1^s by the condition $F_1^s(\pi-\theta)=F_1^s(\theta)$. For even n, $\cos n\theta$ can be written as a sum of products of even powers of $\sin\theta$ and $\cos\theta$ due to the relation $\cos n\theta=\cos^n\theta-\frac{n(n-1)}{2}\sin^2\theta\cos^{n-2}\theta+\cdots$. Because $\cos^2\theta=1-\sin^2\theta$, even powers of $\cos\theta$ can be expressed as sums of even powers of $\sin\theta$. Consequently, $F_1^s(\theta)$ is a sum of even powers of $\sin\theta$. The condition $F_2^s(\pi-\theta)=-F_2^s(\theta)$ rules out $\cos n\theta$ with even n. Due to the relations discussed above, it is clear that $\cos n\theta$ with odd n can be written as $\cos\theta$ times a sum of even powers of $\sin\theta$. Hence, we arrive at the expansion

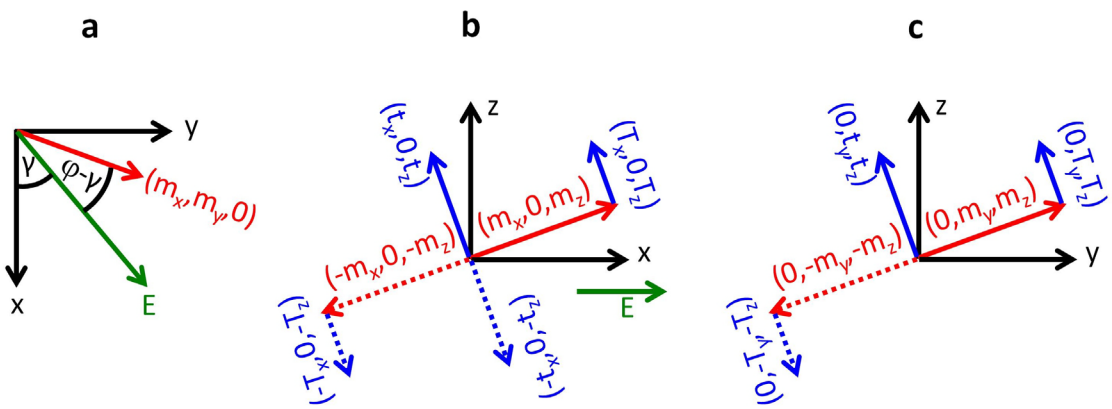

Figure S2. Symmetry properties of the torque. **a,** Angle definitions used in the text. **b,** Effect of mirror reflection at the *xz* plane on the *x* and *z* components of *T* and *m*. Since the electric field *E* is invariant, t_x and t_z undergo the same sign change as T_x and T_z. **c,** Effect of mirror reflection at the *yz* plane on the *y* and *z* components of *T* and *m*. Since *E* (along *x*) changes sign, t_y and t_z are invariant.

$$t_s(\theta,\varphi) = \cos\varphi\,(A_0^s + A_2^s \sin^2\theta + A_4^s \sin^4\theta + \cdots)$$
$$+ \cos\theta \sin\varphi\,(B_0^s + B_2^s \sin^2\theta + B_4^s \sin^4\theta + \cdots)\,. \qquad (11)$$

The torkance $\boldsymbol{t}(\theta,\varphi)$ is the sum of the even and odd parts $\boldsymbol{t}^{\parallel}(\theta,\varphi) = \frac{\boldsymbol{t}(\theta,\varphi)+\boldsymbol{t}(\pi-\theta,\pi+\varphi)}{2}$ and $\boldsymbol{t}^{\perp}(\theta,\varphi) = \frac{\boldsymbol{t}(\theta,\varphi)-\boldsymbol{t}(\pi-\theta,\pi+\varphi)}{2}$, respectively. Due to $\boldsymbol{e}_\varphi(\pi-\theta,\pi+\varphi) = -\boldsymbol{e}_\varphi(\theta,\varphi)$ and $\boldsymbol{e}_\theta(\pi-\theta,\pi+\varphi) = \boldsymbol{e}_\theta(\theta,\varphi)$, the expansions of the even and odd parts of the torque are given by

$$\boldsymbol{t}^{\parallel}(\theta,\varphi) = \cos\varphi\left(A_0^\varphi + A_2^\varphi \sin^2\theta + A_4^\varphi \sin^4\theta + \cdots\right)\boldsymbol{e}_\varphi +$$
$$\cos\theta \sin\varphi\left(B_0^\theta + B_2^\theta \sin^2\theta + B_4^\theta \sin^4\theta + \cdots\right)\boldsymbol{e}_\theta \qquad (12)$$

and

$$\boldsymbol{t}^{\perp}(\theta,\varphi) = \cos\varphi\left(A_0^\theta + A_2^\theta \sin^2\theta + A_4^\theta \sin^4\theta + \cdots\right)\boldsymbol{e}_\theta +$$
$$\cos\theta \sin\varphi\left(B_0^\varphi + B_2^\varphi \sin^2\theta + B_4^\varphi \sin^4\theta + \cdots\right)\boldsymbol{e}_\varphi \qquad (13)$$

An additional requirement is that the torkance shall be independent of φ at $\theta=0$. Since $\cos\varphi\,\boldsymbol{e}_\theta(0,\varphi) - \sin\varphi\,\boldsymbol{e}_\varphi(0,\varphi) = \boldsymbol{e}_x$ and $\sin\varphi\,\boldsymbol{e}_\theta(0,\varphi) + \cos\varphi\,\boldsymbol{e}_\varphi(0,\varphi) = \boldsymbol{e}_y$, this is achieved by imposing $A_0^\varphi = B_0^\theta$ and $A_0^\theta = -B_0^\varphi$, which leads to

$$\boldsymbol{t}^{\parallel}(\theta,\varphi) = \cos\varphi\left(A_0^\varphi + A_2^\varphi \sin^2\theta + A_4^\varphi \sin^4\theta + \cdots\right)\boldsymbol{e}_\varphi +$$
$$\cos\theta \sin\varphi\left(A_0^\varphi + B_2^\theta \sin^2\theta + B_4^\theta \sin^4\theta + \cdots\right)\boldsymbol{e}_\theta \qquad (14)$$

and

$$\boldsymbol{t}^{\perp}(\theta,\varphi) = \cos\varphi\left(A_0^\theta + A_2^\theta \sin^2\theta + A_4^\theta \sin^4\theta + \cdots\right)\boldsymbol{e}_\theta +$$
$$\cos\theta \sin\varphi\left(-A_0^\theta + B_2^\varphi \sin^2\theta + B_4^\varphi \sin^4\theta + \cdots\right)\boldsymbol{e}_\varphi \qquad (15)$$

It is straightforward to verify that Eqs. 14 and 15 lead to the following expression for the torques:

$$\boldsymbol{T}^{\parallel} = \boldsymbol{m} \times [(\boldsymbol{e}_z \times \boldsymbol{E}) \times \boldsymbol{m}]\left[A_0^\varphi + B_2^\theta(\boldsymbol{e}_z \times \boldsymbol{m})^2 + B_4^\theta(\boldsymbol{e}_z \times \boldsymbol{m})^4 + \ldots\right] +$$
$$(\boldsymbol{m} \times \boldsymbol{e}_z)(\boldsymbol{m} \cdot \boldsymbol{E})\left[\left(B_2^\theta - A_2^\varphi\right) + \left(B_4^\theta - A_4^\varphi\right)(\boldsymbol{e}_z \times \boldsymbol{m})^2 + \ldots\right] \qquad (16)$$

and

$$\boldsymbol{T}^{\perp} = (\boldsymbol{e}_z \times \boldsymbol{E}) \times \boldsymbol{m}\left[A_0^\theta - B_2^\varphi(\boldsymbol{e}_z \times \boldsymbol{m})^2 - B_4^\varphi(\boldsymbol{e}_z \times \boldsymbol{m})^4 - \ldots\right] +$$
$$\boldsymbol{m} \times [(\boldsymbol{m} \times \boldsymbol{e}_z)(\boldsymbol{m} \cdot \boldsymbol{E})]\left[\left(A_2^\theta + B_2^\varphi\right) + \left(A_4^\theta + B_4^\varphi\right)(\boldsymbol{e}_z \times \boldsymbol{m})^2 + \ldots\right]. \qquad (17)$$

Notably, $\boldsymbol{T}^{\parallel}$ and $\boldsymbol{T}^{\perp}$ depend explicitly on the three vectors $\boldsymbol{E}$, $\boldsymbol{m}$, and $\boldsymbol{e}_z$, where the presence of $\boldsymbol{e}_z$ reflects the absence of z reflection symmetry. By choosing $\boldsymbol{E}$ (the electric current) to point in the x direction and $|\boldsymbol{E}| = 1$ for simplicity, Eqs. 16 and 17 give

$$\boldsymbol{T}^{\parallel} = \boldsymbol{m} \times (\boldsymbol{e}_y \times \boldsymbol{m})\left[A_0^{\varphi} + B_2^{\theta}(\boldsymbol{e}_z \times \boldsymbol{m})^2 + B_4^{\theta}(\boldsymbol{e}_z \times \boldsymbol{m})^4 + \ldots\right] + (\boldsymbol{m} \times \boldsymbol{e}_z)(\boldsymbol{m} \cdot \boldsymbol{e}_x)\left[\left(B_2^{\theta} - A_2^{\varphi}\right) + \left(B_4^{\theta} - A_4^{\varphi}\right)(\boldsymbol{e}_z \times \boldsymbol{m})^2 + \ldots\right] \quad (18)$$

and

$$\boldsymbol{T}^{\perp} = \boldsymbol{e}_y \times \boldsymbol{m}\left[A_0^{\theta} - B_2^{\varphi}(\boldsymbol{e}_z \times \boldsymbol{m})^2 - B_4^{\varphi}(\boldsymbol{e}_z \times \boldsymbol{m})^4 - \ldots\right] + \boldsymbol{m} \times [(\boldsymbol{m} \times \boldsymbol{e}_z)(\boldsymbol{m} \cdot \boldsymbol{e}_x)]\left[\left(A_2^{\theta} + B_2^{\varphi}\right) + \left(A_4^{\theta} + B_4^{\varphi}\right)(\boldsymbol{e}_z \times \boldsymbol{m})^2 + \ldots\right]. \quad (19)$$

The previous two equations have been used in the main part of the manuscript to give a vector form of the torques. Only the coefficients $A_0^{\varphi} \equiv T_0^{\parallel}$, $A_2^{\varphi} \equiv T_2^{\parallel}$, $A_4^{\varphi} \equiv T_4^{\parallel}$ and $A_0^{\theta} \equiv T_0^{\perp}$, $B_2^{\varphi} \equiv -T_2^{\perp}$, $B_4^{\varphi} \equiv -T_4^{\perp}$, have been retained there, because the others are below the experimental detection limit.

We note that the special case of $A_n^{\varphi} = B_n^{\theta} = 0$ for all $n \neq 0$ leads to

$$\boldsymbol{T}^{\parallel} = A_0^{\varphi}\left(\cos\varphi\, \boldsymbol{e}_{\varphi} + \cos\theta \sin\varphi\, \boldsymbol{e}_{\theta}\right) = A_0^{\varphi}\left[\left(\boldsymbol{e}_y \cdot \boldsymbol{e}_{\varphi}\right)\boldsymbol{e}_{\varphi} + \left(\boldsymbol{e}_y \cdot \boldsymbol{e}_{\theta}\right)\boldsymbol{e}_{\theta}\right] = A_0^{\varphi}\left[\boldsymbol{e}_y - (\boldsymbol{e}_y \cdot \boldsymbol{m})\boldsymbol{m}\right] = A_0^{\varphi}\boldsymbol{m} \times (\boldsymbol{e}_y \times \boldsymbol{m}) \quad (20)$$

and, likewise, the special case of $A_n^{\theta} = B_n^{\varphi} = 0$ for all $n \neq 0$ simplifies $\boldsymbol{T}^{\perp}$ to

$$\boldsymbol{T}^{\perp} = A_0^{\theta}\left(\cos\varphi\, \boldsymbol{e}_{\theta} - \cos\theta \sin\varphi\, \boldsymbol{e}_{\varphi}\right) = A_0^{\theta}\left(\cos\varphi\, \boldsymbol{e}_{\varphi} + \cos\theta \sin\varphi\, \boldsymbol{e}_{\theta}\right) \times \boldsymbol{m} = A_0^{\theta}\left[\boldsymbol{m} \times (\boldsymbol{e}_y \times \boldsymbol{m})\right] \times \boldsymbol{m} = A_0^{\theta}(\boldsymbol{e}_y \times \boldsymbol{m}) . \quad (21)$$

These reduced expressions have been obtained theoretically for several models discussed in the literature (see main text).

For the purpose of comparison with the experiment, it is useful to derive the effective magnetic fields $\boldsymbol{B}^I(\theta, \varphi)$ associated with the torques. Since $\boldsymbol{T} = \boldsymbol{m} \times \boldsymbol{B}^I$, by multiplying the previous equation by $\boldsymbol{m}$ and noting that $(\boldsymbol{m} \times \boldsymbol{B}^I) \times \boldsymbol{m} = \boldsymbol{B}^I(\boldsymbol{m} \cdot \boldsymbol{m}) - \boldsymbol{m}(\boldsymbol{m} \cdot \boldsymbol{B}^I) = \boldsymbol{B}^I$, one has $\boldsymbol{B}^I = \boldsymbol{T} \times \boldsymbol{m}$. The effective fields corresponding to $\boldsymbol{T}^{\parallel}$ and $\boldsymbol{T}^{\perp}$are

$$\boldsymbol{B}^{\parallel} = (\boldsymbol{e}_y \times \boldsymbol{m})\left[A_0^{\varphi} + B_2^{\theta}(\boldsymbol{e}_z \times \boldsymbol{m})^2 + B_4^{\theta}(\boldsymbol{e}_z \times \boldsymbol{m})^4 + \ldots\right] + (\boldsymbol{m} \times \boldsymbol{e}_z) \times \boldsymbol{m}(\boldsymbol{m} \cdot \boldsymbol{e}_x)\left[\left(B_2^{\theta} - A_2^{\varphi}\right) + \left(B_4^{\theta} - A_4^{\varphi}\right)(\boldsymbol{e}_z \times \boldsymbol{m})^2 + \ldots\right] \quad (22)$$

and

$$\boldsymbol{B}^{\perp} = \left(\boldsymbol{e}_y \times \boldsymbol{m}\right) \times \boldsymbol{m}\left[A_0^{\theta} - B_2^{\varphi}(\boldsymbol{e}_z \times \boldsymbol{m})^2 - B_4^{\varphi}(\boldsymbol{e}_z \times \boldsymbol{m})^4 - \ldots\right] +$$

$$(\boldsymbol{m} \times \boldsymbol{e}_z)(\boldsymbol{m} \cdot \boldsymbol{e}_x)\left[\left(A_2^{\theta} + B_2^{\varphi}\right) + \left(A_4^{\theta} + B_4^{\varphi}\right)(\boldsymbol{e}_z \times \boldsymbol{m})^2 + \ldots\right]. \quad (23)$$

These expressions are valid also for the spin accumulation, since $\delta\boldsymbol{m}^{\parallel} \sim \boldsymbol{B}^{\parallel}$ and $\delta\boldsymbol{m}^{\perp} \sim \boldsymbol{B}^{\perp}$. In spherical coordinates, using $\boldsymbol{e}_\theta \times \boldsymbol{m} = -\boldsymbol{e}_\varphi$ and $\boldsymbol{e}_\varphi \times \boldsymbol{m} = \boldsymbol{e}_\theta$, we obtain

$$\boldsymbol{B}^{\parallel}(\theta,\varphi) = \cos\varphi\left(A_0^{\varphi} + A_2^{\varphi}\sin^2\theta + A_4^{\varphi}\sin^4\theta + \cdots\right)\boldsymbol{e}_\theta -$$

$$\cos\theta\sin\varphi\left(A_0^{\varphi} + B_2^{\theta}\sin^2\theta + B_4^{\theta}\sin^4\theta + \cdots\right)\boldsymbol{e}_\varphi \quad (24)$$

and

$$\boldsymbol{B}^{\perp}(\theta,\varphi) = -\cos\varphi\left(A_0^{\theta} + A_2^{\theta}\sin^2\theta + A_4^{\theta}\sin^4\theta + \cdots\right)\boldsymbol{e}_\varphi +$$

$$\cos\theta\sin\varphi\left(-A_0^{\theta} + B_2^{\varphi}\sin^2\theta + B_4^{\varphi}\sin^4\theta + \cdots\right)\boldsymbol{e}_\theta. \quad (25)$$

The polar and azimuthal components of the total effective field $\boldsymbol{B}^I = \boldsymbol{B}^{\parallel}(\theta,\varphi) + \boldsymbol{B}^{\perp}(\theta,\varphi)$ are then given by

$$B_\theta(\theta,\varphi) = \cos\varphi\left(A_0^{\varphi} + A_2^{\varphi}\sin^2\theta + A_4^{\varphi}\sin^4\theta + \cdots\right) +$$

$$\cos\theta\sin\varphi\left(-A_0^{\theta} + B_2^{\varphi}\sin^2\theta + B_4^{\varphi}\sin^4\theta + \cdots\right) \quad (26)$$

and

$$B_\varphi(\theta,\varphi) = -\cos\varphi\left(A_0^{\theta} + A_2^{\theta}\sin^2\theta + A_4^{\theta}\sin^4\theta + \cdots\right) -$$

$$\cos\theta\sin\varphi\left(A_0^{\varphi} + B_2^{\theta}\sin^2\theta + B_4^{\theta}\sin^4\theta + \cdots\right). \quad (27)$$

We conclude this section by noting that Eqs. 22, 23 determine only the components of the effective field which are perpendicular to $\boldsymbol{m}$. In general, however, even though effective fields along the magnetization direction do not produce any torques, it is expected that the current also induces fields parallel to $\boldsymbol{m}$. While such a radial component of the current-induced magnetic field ($\boldsymbol{B}_r$) is not accessible in the present experiment, we provide below its most general expression compatible with the symmetry of the system. By extending the analysis for the torque presented above to the effective field, one can show that

$$\boldsymbol{B}_r(\theta,\varphi) = [\sin\theta\cos\theta\cos\varphi\,(A_0^r + A_2^r\sin^2\theta + A_4^r\sin^4\theta + \cdots) +$$

$$\sin\theta\sin\varphi(B_0^r + B_2^r\sin^2\theta + B_4^r\sin^4\theta + \cdots)]\boldsymbol{m}\,. \quad (28)$$

S2. Harmonic analysis of the Hall voltage

We use the Hall voltage (V_H) to measure the behaviour of the magnetization as a function of external field and current-induced torques. In general, one has

$$V_H = IR_H = R_{AHE} I \cos\theta + R_{PHE} I \sin^2\theta \sin 2\varphi, \qquad (29)$$

where I is the current and R_H the Hall resistance due to the anomalous Hall effect (AHE) and planar Hall effect (PHE). We omit here the ordinary Hall effect, which is negligible in ferromagnetic materials, as well as thermoelectric effects, which will be discussed in Section S7. The AHE is proportional to $R_{AHE} I \cos\theta$ and the PHE to $R_{PHE} I \sin^2\theta \sin 2\varphi$, where R_{AHE} and R_{PHE} are the AHE and PHE resistances, θ and φ the polar and azimuthal angle of the magnetization, respectively, as defined in Fig.1b of the main text. Due to the presence of effective fields, the injection of a moderate ac current $I_{ac} = Ie^{i2\pi ft}$ induces small oscillations of the magnetization around its equilbrium position (θ_0, φ_0), defined by the anisotropy field B_k and external field B_{ext}. These oscillations modulate R_H giving rise to a time-dependent Hall voltage signal. After simplification of the time-dependent phase factor, the dependence of the Hall voltage on the current can be expanded to first order as

$$V_H(I) \approx V_H(\theta_0, \varphi_0) + I \left.\frac{dV_H}{dI}\right|_{\theta_0,\varphi_0}. \qquad (30)$$

Straightforward differentiation of Eq. 29, keeping into account that both θ and φ depend on I, gives $\frac{dV_H}{dI} = R_H^f + R_H^{2f}(I)$, where the first and second harmonic Hall resistance components are given by

$$R_H^f = R_{AHE} \cos\theta_0 + R_{PHE} \sin^2\theta_0 \sin 2\varphi_0 \qquad (31)$$

and

$$R_H^{2f} = I(R_{AHE} - 2R_{PHE} \cos\theta_0 \sin 2\varphi_0) \left.\frac{d\cos\theta}{dI}\right|_{\theta_0} + IR_{PHE} \sin^2\theta_0 \left.\frac{d\sin 2\varphi}{dI}\right|_{\varphi_0}. \qquad (32)$$

We notice that R_H^f is equivalent to the Hall resistance measured in conventional dc measurements, whereas R_H^{2f} contains two terms that depend explicitly on the current. This dependence can be expressed in terms of the current-induced effective field $\boldsymbol{B}^I = \boldsymbol{B}^{\parallel} + \boldsymbol{B}^{\perp} + \boldsymbol{B}^{Oersted}$ by noting that

$$\frac{d\cos\theta}{dI} = \frac{d\cos\theta}{d\boldsymbol{B}^I} \cdot \frac{d\boldsymbol{B}^I}{dI} = \frac{d\cos\theta}{dB_\theta^I}\, b_\theta \qquad (33)$$

and

$$\frac{d\sin 2\varphi}{dI} = \frac{d\sin 2\varphi}{d\boldsymbol{B}^I} \cdot \frac{d\boldsymbol{B}^I}{dI} = \frac{d\sin 2\varphi}{dB_\varphi^I}\, b_\varphi\,, \qquad (34)$$

where B_θ^I and B_φ^I indicate the polar and azimuthal components of $\mathbf{B}^I$ and b_θ and b_φ their derivative with respect to the current. The radial component of $\mathbf{B}^I$ cannot affect the motion of the magnetization and is thus irrelevant to the discussion of the torques. To measure quantitatively the effective fields b_θ and b_φ by means of Eq. 32 we need first to calculate the derivatives of $\cos\theta$ and $\sin 2\varphi$ that appear in Eqs. 33 and 34. As the magnetic field dependence of $\cos\theta$ and $\sin 2\varphi$ (proportional to m_z and $m_x m_y$, respectively) is independent on the nature of the field, we can replace $\mathbf{B}^I$ by $\mathbf{B}_{ext}$ in the derivatives and obtain

$$\frac{d\cos\theta}{dI} = \frac{d\cos\theta}{dB_{ext}} \frac{1}{\sin(\theta_B - \theta_0)} b_\theta\,, \qquad (35)$$

$$\frac{d\sin 2\varphi}{dI} = \frac{d\sin 2\varphi}{dB_\varphi^I}\, b_\varphi = 2\cos 2\varphi \frac{d\varphi}{dB_\varphi^I} b_\varphi \approx \frac{2\cos 2\varphi}{B_{ext}\sin\theta_B}\, b_\varphi\,, \qquad (36)$$

where θ_B is the polar angle defining the direction of $\mathbf{B}_{ext}$. Note that the last relation is exact in the case of uniaxial magnetic anisotropy. Using these expressions, R_H^{2f} can be written as

$$R_H^{2f} = I(R_{AHE} - 2R_{PHE}\cos\theta_0 \sin 2\varphi_0) \left.\frac{d\cos\theta}{dB_{ext}}\right|_{\theta_0} \frac{1}{\sin(\theta_B - \theta_0)} b_\theta + I R_{PHE} \sin^2\theta_0 \frac{2\cos 2\varphi_0}{B_{ext}\sin\theta_B}\, b_\varphi\,. \qquad (37)$$

Equation 34 is valid for any arbitrary field $\mathbf{B}^I$, $\mathbf{B}_{\text{ext}}$, orientation of $\boldsymbol{m}$, and uniaxial magnetic anisotropy, which makes it very useful in the investigation of SOTs.

S3. Separation of AHE and PHE

To make correct use of Eq. 37, it is desirable to measure R_{PHE} in order to separate the PHE and AHE contributions to the total Hall resistance. This can be readily achieved by measuring R_H^f as a function of the external field applied at angles $\varphi \neq$ 0º, 90º. Figure S3a shows R_H^f

measured at $\theta_B = 80°$, $\varphi = 50°$ by means of example. Due to the PHE, which is even with respect to magnetization reversal, the endpoints of the hysteresis loop are asymmetric. As the AHE is odd with respect to magnetization reversal, the first harmonic contributions of the AHE and PHE, R_f^{AHE} and R_f^{PHE}, can be separated by antisymmetrization and symmetrization of R_H^f, respectively. This is achieved in practice by inverting $R_H^f(-B_{ext} \rightarrow +B_{ext})$ with respect to the origin of the curve and taking the sum or difference with $R_H^f(+B_{ext} \rightarrow -B_{ext})$, as shown in Fig. S3b and c, respectively. Macrospin simulations of the AHE and PHE further demonstrate that

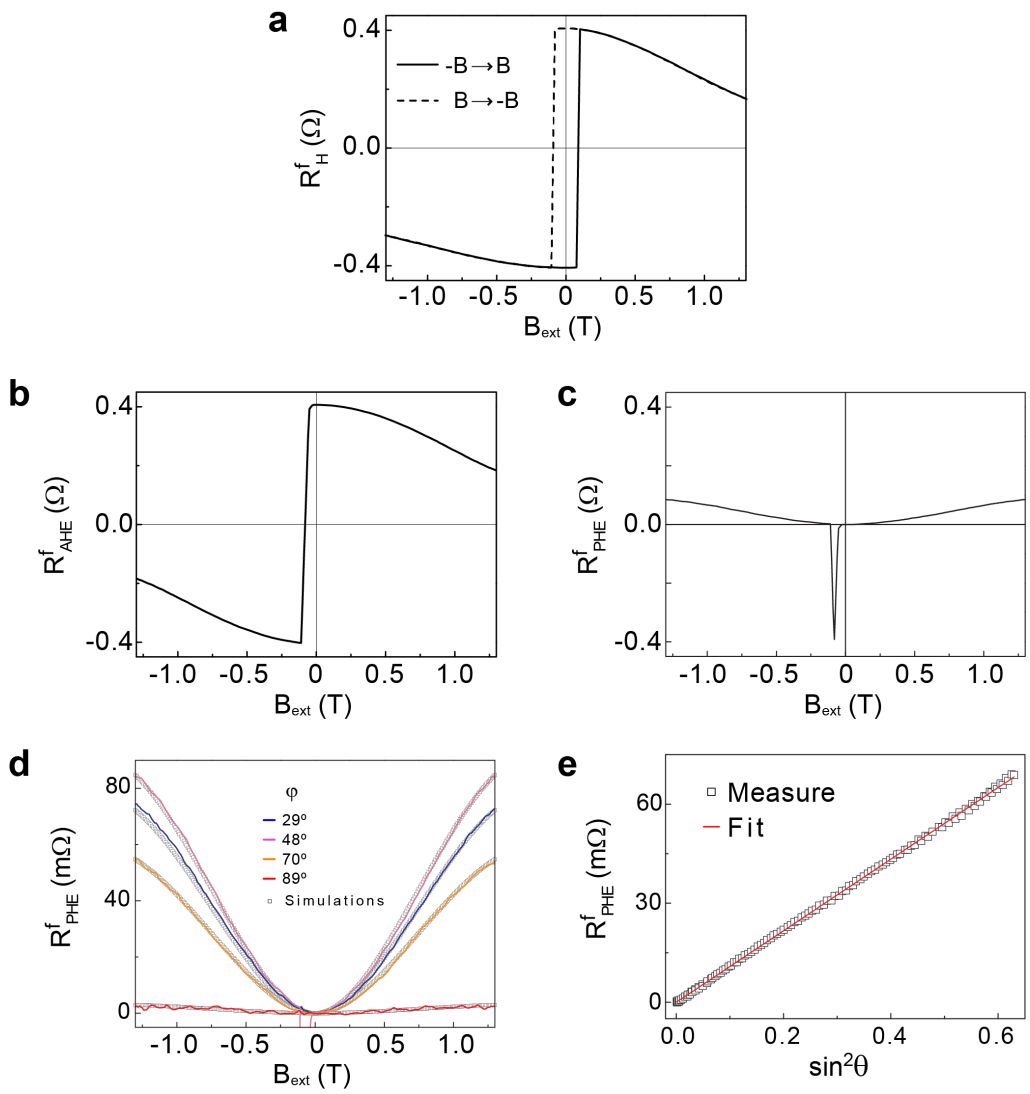

Figure S3. Separation of AHE and PHE. a, First harmonic Hall resistance, R_H^f, measured at $\theta_B = 80°$, $\varphi = 50°$ and $I = 600$ mA. **b,** Antisymmetric AHE signal, R_{AHE}^f. **c,** Symmetric PHE signal, R_{PHE}^f. **d,** Comparison between macrospin simulations (dots) and measurements (solid lines) of R_{PHE}^f at different angles φ. **e,** R_f^{PHE} as a function of $\sin^2\theta$ showing the expected linear dependence. The slope of this curve gives the PHE resistance, $R_{PHE} = 0.11\ \Omega$.

this procedure yields correct quantitative results, as shown in Fig. S3d. Finally, the PHE saturation resistance is deduced from the linear fit of R_f^{PHE} vs. $\sin^2\theta_M$ (Fig. S3e). For this sample, we obtain $R_{PHE} = 0.11\ \Omega$. The saturation value of the AHE resistance is $R_{AHE} = 0.81\ \Omega$. Finally, R_f^{AHE} is employed to calculate the equilibrium angle of the magnetization (θ_0) at each value of the applied field using the relationship

$$\theta_0 = \mathrm{acos}\left|\frac{R_f^{AHE}(B_{ext})}{R_{AHE}}\right|. \qquad (38)$$

S4. Measurement of an external ac field using the Hall voltage

The measurements of the effective fields based on the harmonic analysis of the Hall voltage described above have been quantitatively checked by applying an ac magnetic field of known amplitude and retrieving its value using Eqs. 37 and 38. To this end, we modulated B_{ext} by a small sinusoidal field of amplitude B_{ac} = 10.5 mT at a frequency of 1 Hz. The current frequency was also set to f = 1 Hz in order to match the modulation frequency of the electromagnet. The polar component of the ac field acting on the magnetization in this case is given by $b_\theta I + B_{ac}\sin(\theta_B - \theta)$. Since b_θ and B_{ac} are independent of each other, R_H^{2f} is given by the sum of $R_H^{2f}(b_\theta)$ and $R_H^{2f}(B_{ac})$. By applying the ac field in-phase or out-of-phase with the current, we measure $R_H^{2f}(b_\theta, b_\varphi, B_{ac}) = R_H^{2f}(b_\theta, b_\varphi) + R_H^{2f}(B_{ac})$ and $R_H^{2f}(b_\theta, b_\varphi, -B_{ac}) = R_H^{2f}(b_\theta, b_\varphi) - R_H^{2f}(B_{ac})$, respectively (Fig. S4a). This allows us to separate the two contributions $R_H^{2f}(b_\theta, b_\varphi)$ and $R_H^{2f}(B_{ac})$ by taking the sum and difference of the above relationships. As expected, $R_H^{2f}(b_\theta, b_\varphi)$ coincides with the measurement of R_H^{2f} in the absence of ac field (Fig. S4b). To calculate the amplitude B_{ac} from the experimental data, we use Eq. 37, which leads to

$$B_{ac} = -\frac{2R_H^{2f}(B_{ac})}{(R_{AHE} - 2R_{PHE}\cos\theta_0\sin 2\varphi_0)\dfrac{d\cos\theta}{dB_{ext}}} \qquad (39)$$

The term $\frac{d\cos\theta}{dB_{ext}}$ can be evaluated from the numerical derivative of $\frac{1}{R_{AHE}}\frac{dR_f^{AHE}}{dB_{ext}}$ or, equivalently, from $-2R_H^{2f}(B_{ac})$, as demonstrated experimentally in Fig. S4c. We present three measurements of $R_H^{2f}(B_{ac})$ recorded at φ = 90º, 60º, and 0º (Fig. S4d). We note that the curves measured at φ = 90º and φ = 0º have the same shape, whereas the curve measured at φ = 60º is asymmetric due to the contribution of the PHE at this angle. Using Eq. 39, we show that we recover correctly the amplitude B_{ac} = 10.5 mT independently of φ (Fig. S4e), confirming the consistency of the

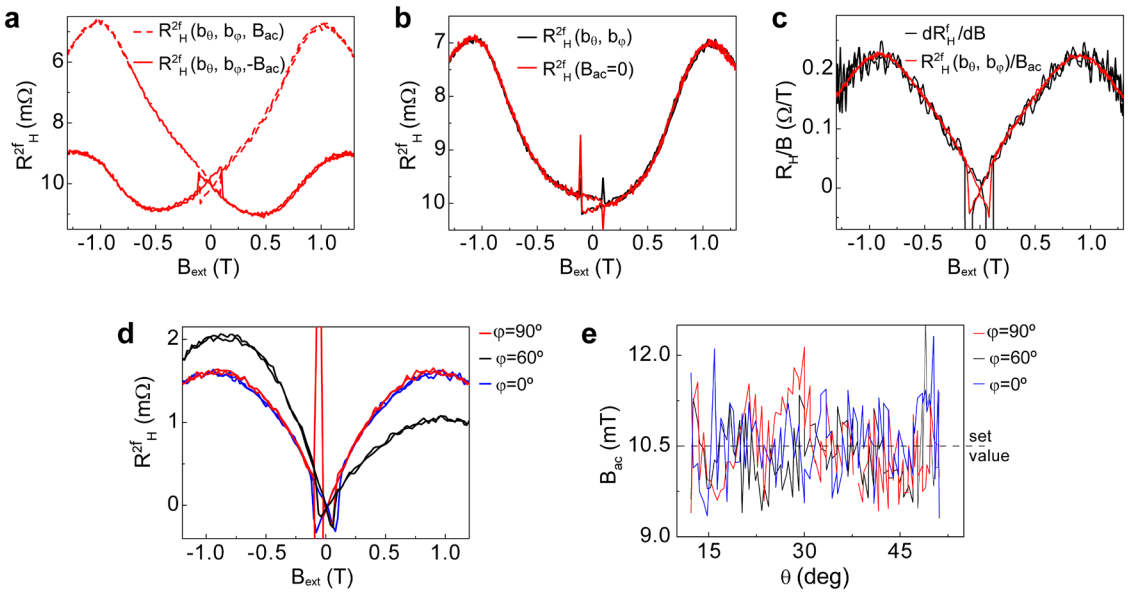

Figure S4. Measurement of an external ac field using the Hall voltage. a, R_H^{2f} measured in-phase (dashed line) and antiphase (solid line) with an applied ac magnetic field parallel to $\mathbf{B}_{ext}$. **b,** Comparison between $R_H^{2f}(b_\theta, b_\varphi)$=$[R_H^{2f}(b_\theta, b_\varphi, B_{ac}) + R_H^{2f}(b_\theta, b_\varphi, -B_{ac})]/2$ (black line) and $R_H^{2f}(b_\theta, b_\varphi, B_{ac} = 0)$ (red line). **c,** Comparison between the numerical derivative of R_{AHE}^f with respect to the applied field (black line) and $R_H^{2f}(B_{ac}) = [R_H^{2f}(b_\theta, b_\varphi, B_{ac}) - R_H^{2f}(b_\theta, b_\varphi, -B_{ac})]/2$ (red line). **d,** $R_H^{2f}(B_{ac})$ recorded at φ = 90º, 60º, and 0º. **e,** Measured amplitude of the applied ac field as a function of magnetization tilt obtained from the curves shown in **d** using Eqs. 38 and 39.

harmonic analysis of the AHE and PHE contributions presented in Sects. 2 and 3. The standard deviation of the data in Fig. S4e is 0.6 mT, which corresponds to a relative error of about 6% on our measurements.

The external ac field is also useful to determine the direction of $\boldsymbol{B}^\perp$ with respect to the Oersted field. In the measurements reported in Fig. S4, $\mathbf{B}_{ext}$ is perpendicular to the current and, when positive, it is opposite to the Oersted field generated by a positive current flowing in the Pt layer. The Oersted field is determined by the conventional right-hand rule. In Fig. S4a we observe that R_H^{2f} increases (decreases) when B_{ac} is in-phase (out-of-phase) with the current, meaning that B^{odd} and B_{ac} add up for an in-phase measurement, i.e., that $\boldsymbol{B}^\perp$ is positive for a positive current. Therefore, we conclude that $\boldsymbol{B}^\perp$ is opposite to the Oersted field.

S5. Measurement of current-induced effective fields in the case of nonzero PHE

Equation 37 relates R_H^{2f} to the effective field components b_θ and b_φ. If the PHE is neglected, b_θ reads

$$b_\theta = \frac{R_H^{2f}\sin(\theta_B - \theta_0)}{IR_{AHE}\left.\frac{d\cos\theta}{dB_{ext}}\right|_{\theta_0}}, \qquad (40)$$

which is readily evaluated by noting that

$$R_{AHE}\left.\frac{d\cos\theta}{dB_{ext}}\right|_{\theta_0} = \left.\frac{dR_H^f}{dB_{ext}}\right|_{\theta_0}. \qquad (41)$$

However, despite the fact that the PHE is significantly smaller than the AHE in AlOx/Co/Pt, we find that neglecting the PHE affects the quantitative determination of b_θ and, therefore, of $B^\perp$ and $B^\parallel$. In fact, Eq. 40 does not allow for a precise calculation of the current-induced fields and one must resort to the more general Eq. 37. In order to solve Eq. 37 for b_θ and b_φ, we thus use a recursive procedure that takes advantage of the indipendent measurement of R_{PHE} and R_{AHE} reported in Sect. 3. Starting from R_H^{2f} measured at $\varphi = 0°$ and 90° (blue curves in Fig. S5a and b, respectively) we operate as follows:

i) We set $R_{PHE} = 0$ as initial guess and evaluate $b_\theta^0(\varphi = 90°)$ and $b_\varphi^0(\varphi = 0°)$, shown in black in Fig. S5 a and c, respectively.

ii) We set R_{PHE} to its measured value and evaluate $b_\theta^1(\varphi = 90°)$ using the previous estimate of $b_\varphi^0(\varphi = 0°)$. Using both further gives $b_\varphi^1(\varphi = 0°)$.

iii) We evaluate $b_\theta^1(\varphi = 0°)$ using $b_\varphi^1(\varphi = 0°)$, which further gives $b_\varphi^1(\varphi = 90°)$, as shown in Fig. S5 b,d, blue curves.

iv) Steps ii) and iii) are repeated until we achieve convergence (red curves in Fig. S5).

Figures S5c and d show the successive iterations that lead to the final form of b_θ at $\varphi = 90°$ and 0°, respectively. This procedure is independent on the choice of coefficients used to represent b_θ and b_φ.

We note that Eqs. 24-27 imply that $b_\theta = B^\perp$ at $\varphi = 90°$ and $b_\theta = B^\parallel$ at $\varphi = 0°$. Recalling that by truncating the angular expansion of the torques to fourth order we have

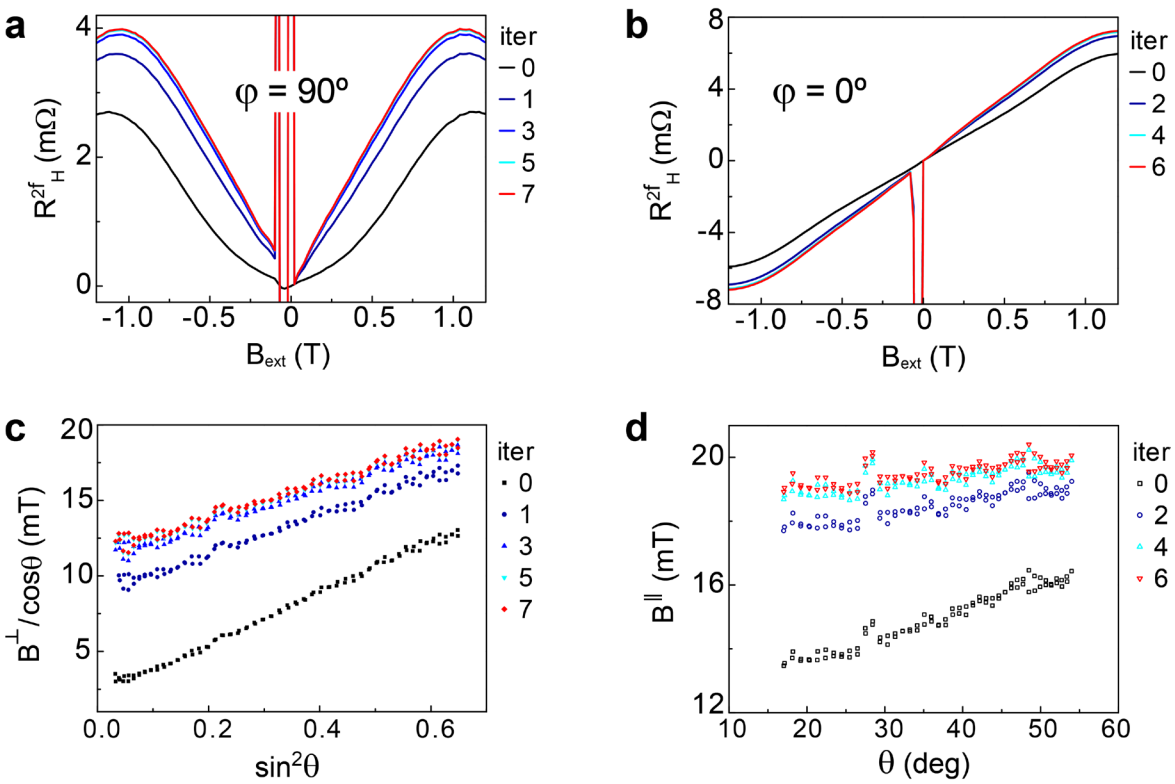

Figure S5. Recursive procedure to determine $B^{\perp}$ and $B^{\parallel}$ in the case of nonzero PHE. **a,** R_H^{2f} measured at $\varphi = 90°$ (black line) and successive iterations that lead to the separation of the pure AHE contribution $R_{AHE}^{2f}(\varphi = 90°)$ (red line). **b,** R_H^{2f} measured at $\varphi = 0°$ (black line) and successive iterations that lead to $R_{AHE}^{2f}(\varphi = 0°)$ (red line). **c,** Iterations leading to convergent $B^{\perp}$ values at $\varphi = 0°$. **d,** Iterations leading to convergent $B^{\parallel}$ values at $\varphi = 0°$.

$$Ib_\theta(\varphi = 0°) = T_0^{\parallel} + T_2^{\parallel}\sin^2\theta + T_4^{\parallel}\sin^4\theta, \tag{42}$$

$$Ib_\theta(\varphi = 90°) = -\cos\theta\,(T_0^{\perp} + T_2^{\perp}\sin^2\theta + T_4^{\perp}\sin^4\theta), \tag{43}$$

$$Ib_\varphi(\varphi = 0°) = -T_0^{\perp}, \tag{44}$$

$$Ib_\varphi(\varphi = 90°) = -\cos\theta\, T_0^{\parallel}, \tag{45}$$

the values of the coefficients $T_{0,2,4}^{\parallel}$ and $T_{0,2,4}^{\perp}$ are obtained by fitting $b_\theta(\varphi = 0°)$ and $b_\theta(\varphi = 90°)$ using Eqs. 42 and 43.

S6. Macrospin simulations

To validate the iteration procedure described above, we performed numerical simulations using a macrospin model that includes the effects of SOTs. The model allows us to simulate R_H^f and R_H^{2f} as a function of B_{ext} starting from the equilibrium equation for the magnetization:

$$\boldsymbol{m} \times \boldsymbol{B}_{ext} + \boldsymbol{m} \times \boldsymbol{B}_k + \boldsymbol{T}^{\perp} + \boldsymbol{T}^{\parallel} = 0\,, \qquad (46)$$

where the first term represents the torque due to the external field and the second term the torque due to the anisotropy field $\boldsymbol{B}_k = [B_{k1}(\boldsymbol{m}\cdot\boldsymbol{z}) + B_{k2}(\boldsymbol{m}\cdot\boldsymbol{z})^3]\boldsymbol{z}$, with second and fourth order anisotropy constants B_{k1} = -0.95 T and B_{k2} = -0.2 T, respectively. We assume here the simplest form of $\boldsymbol{T}^{\perp}$ and $\boldsymbol{T}^{\parallel}$ compatible with the experimental results of AlO_x/Co/Pt, namely

$$\boldsymbol{T}^{\perp} = \cos\phi\, T_0^{\perp}\mathbf{e}_\theta - \cos\theta\sin\phi\,(T_0^{\perp} + T_2^{\perp}\sin^2\theta)\mathbf{e}_\phi \qquad (47)$$

and

$$\boldsymbol{T}^{\parallel} = \cos\theta\sin\phi\, T_0^{\parallel}\mathbf{e}_\theta + \cos\phi T_0^{\parallel}\,\mathbf{e}_\phi \qquad (48)$$

and set the SOT coefficients to $T_0^{\perp}$ = -12.0 mT, $T_2^{\perp}$ = -11.0 mT, and $T_0^{\parallel}$ = 19.0 mT. These coefficients are modulated by the current, which is proportional to $e^{i2\pi ft}$. By solving Eq. 43 at each instant t for the angles θ_0 and φ_0 that define the equilibrium direction of $\boldsymbol{m}$ and taking R_{AHE} = 0.8 Ω and R_{PHE} = 0.09 Ω, we calculate $V_H(t)$ using Eq. 29.Then, $V_H(t)$ is Fourier-transformed to obtain R_H^f and R_H^{2f} as a function of B_{ext}. Figure S6a and b show that the simulations faithfully reproduce the shape of the experimental R_H^{2f} curves measured at φ = 0º and 90º, respectively (see Fig. 2, main text). Further, by applying the iteration steps i-iv described above to the simulated data (Fig. S6c-f), we find a very similar convergence behaviour to that reported for the experimental data in Fig. S5. Moreover, after a maximum of seven iteration steps, we recover the values $T_0^{\perp}$ = -11.99 mT, $T_2^{\perp}$ = -11.01 mT, and $T_0^{\parallel}$ = 18.97 mT, thus confirming the validity of our analysis.

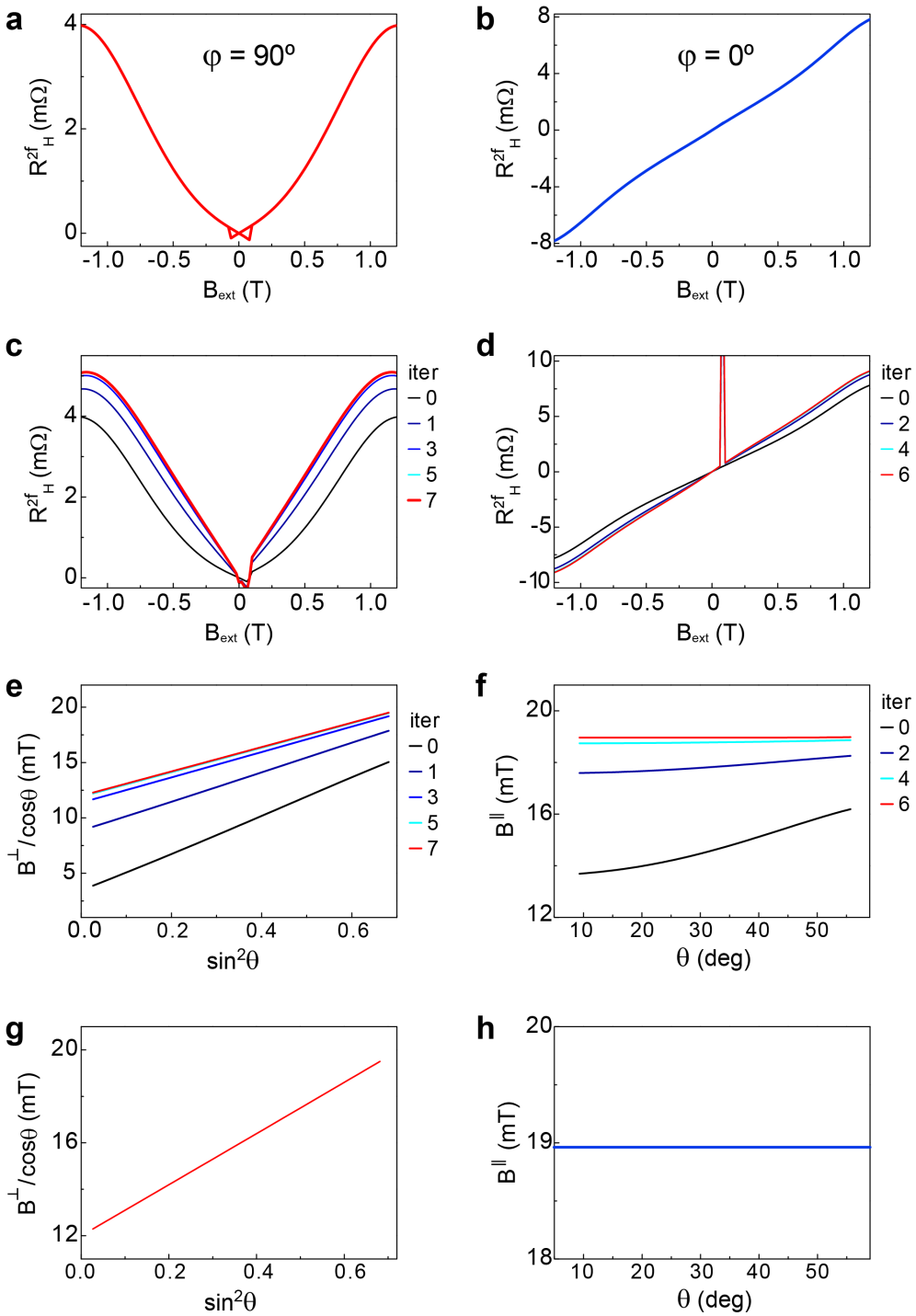

Figure S6. Macrospin simulations of R_H^{2f}, $B^{\perp}$, and $B^{\parallel}$ including both the AHE and PHE contributions to the Hall voltage. a, Simulated R_H^{2f} signal at $\varphi = 90°$ and **b,** $\varphi = 0°$ (see text for details). **c, d,** Iteration procedure to separate the pure AHE components (**c**) $R_{AHE}^{2f}(\varphi = 90°)$ and (**d**) $R_{AHE}^{2f}(\varphi = 0°)$ applied to the simulated signal. Iterative estimate of **e,** $B^{\perp}$ at $\varphi = 0°$ and **f,** $B^{\parallel}$ at $\varphi = 0°$. Final result for **g,** $B^{\perp}$ and **h,** $B^{\parallel}$ derived from the macrospin simulation of the Hall voltage and analysis of the second harmonic AHE and PHE. $B^{\perp}$ and $B^{\parallel}$ coincide with the input values assumed in the simulations.

S7. Sample-dependent offset and Nernst-Ettingshausen effect

Aside from the AHE and PHE, the measurement of R_H^{2f} is sensitive to sample-dependent contributions to the Hall voltage, namely the misalignment of the voltage leads and thermoelectric effects.[2] The current flowing into the Hall cross can generate a temperature gradient due to inhomogeneous heating in correspondence of fabrication defects, generally on the corners of the sample. This gradient induces two types of thermoelectric voltages, the Seebeck effect and the Anomalous Nernst-Ettingshausen effect (ANE). Since heating is modulated by the ac current, we detect both contributions in the *2f* component of the Hall voltage. We note that these effects vary in amplitude and sign from sample to sample and that, once accounted for, R_H^{2f} presents the same magnetization dependence in all samples.

The largest sample-dependent contribution to R_H^{2f} is a constant offset (R_{Offset}) due to the asymmetry of the voltage probes as well as to the Seebeck effect. The ANE, on the other hand, gives a contribution to R_H^{2f} that is magnetization dependent and induces a small asymmetry in the raw R_H^{2f} curves. The voltage induced by ANE is perpendicular to the temperature gradient and m_z, mimicking the AHE with much smaller amplitude. (Fig. S7a and b). Both the offset and

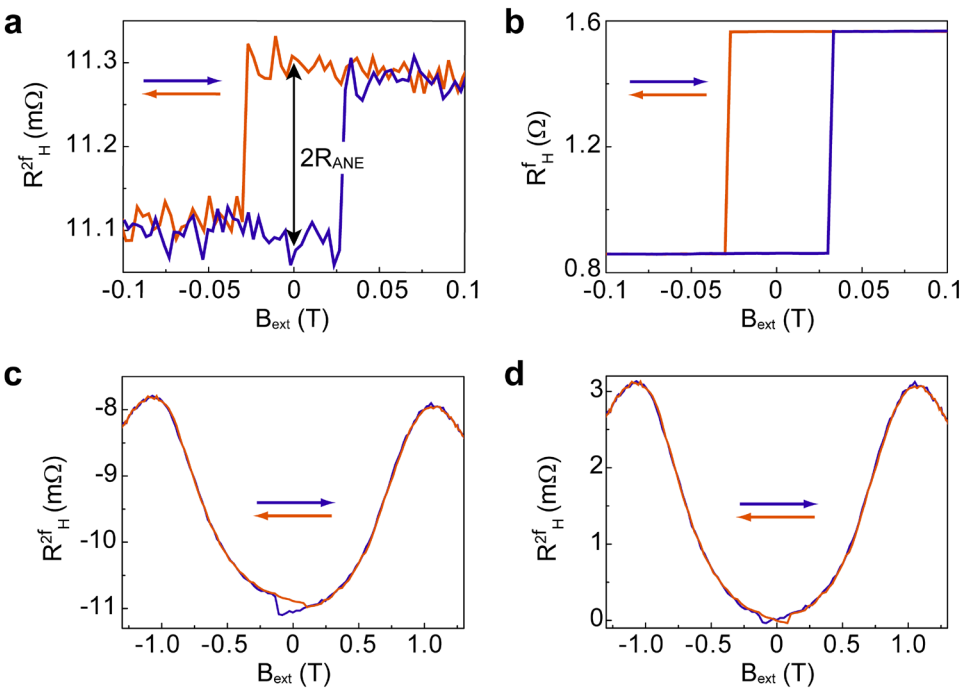

Figure S7. Measurement and subtraction of the Anomalous Nernst effect. a, R_H^{2f} measured at $\theta_B = 0°$, $\varphi = 90°$, and $I = 635$ μA. **b,** R_H^{f} simultaneously measured with **a**. **c, d,** R_H^{2f} measured at $\theta_B = 85°$, $\varphi = 90°$, and $I = 635$ μA before (**c**) and after (**d**) subtraction of the ANE and constant offset.

ANE contributions to R_H^{2f} can be determined by performing a measurement with $\mathbf{B}_{ext}$ // $\mathbf{z}$, as shown in Fig. S7a. In this case, the SOT and Oersted fields do not contribute to the second harmonic signal since the variation of the Hall resistance is symmetric with respect to θ=0°. Hence, the residual R_H^{2f} signal is related uniquely to R_{Offset} and the ANE. As expected for the ANE, R_H^{2f} is hysteretic and has the same field dependence of R_H^f, which is proportional to m_z. One can easily deduce the amplitude of the ANE, R_{ANE}, by taking the difference between the extrema of R_H^{2f} measured for $\mathbf{B}_{ext}$ // $\mathbf{z}$. We find R_{ANE} = 0.1 mΩ for a current of 635 μA, which is comparable with other values found in the literature.[3] For arbitrary orientation of $\mathbf{B}_{ext}$, we find that R_{ANE} coincides with the difference of R_H^{2f} measured at zero field for positive and negative sweeps of B_{ext}, whereas their average gives R_{Offset}. Finally, both R_{Offset} and R_{ANE} can be subtracted from the raw data, giving:

$$R_H^{2f} = R_{raw}^{2f} - R_{ANE}\frac{R_H^f}{2R_{AHE}} - R_{Offset} \ . \qquad (49)$$

Figures S7c and d show R_H^{2f} before and after subtraction of R_{Offset} and ΔR_{ANE}, respectively.

S8. Current dispersion in the Hall voltage probes

The SOT/current ratios reported in the main text are calculated without taking into account the spread of the charge current into the voltage leads of the Hall cross. Depending on the relative width of the Hall voltage probes with respect to the current probes, the actual current giving rise to the SOTs may be smaller than the total current injected into the device. Numerical simulations of the current flow in a Hall cross show that the current density in the central region of the cross reduces by up to 23% (8%) in junctions where the width of the voltage probes is equal (half) the width of the current probes.[4] The dimensions of the Hall cross in our devices are 500 x 500 nm^2, 1000 x 1000 nm^2, and 1000 x 500 nm^2. Figure 3 in the main text shows that the SOT/current ratios measured in the 500 x 500 nm^2 and 1000 x 1000 nm^2 devices are similar, whereas in the 1000 x 500 nm^2 device they are larger by 20-30% relative to the symmetric probes. Figure S8 shows a set of measurements for a 1000 x 500 nm^2 device of AlO_x/Co/Pt recorded at φ = 90º, 0º, and θ_B = 82º. For an ac current amplitude set to I = 1040 μA, corresponding to a current density j = 2.91x10^{7}A/cm^2, we obtain $T_0^{\perp}$ = -16 ± 1 mT, $T_2^{\perp}$ = -12.8 ± 0.8 mT, and $T_0^{\parallel}$ = 25 ± 1 mT. For a 1000 x 1000 nm^2 device patterned on the same wafer, we measured $T_0^{\perp}$ = -11.4 mT, $T_2^{\perp}$ = -9.3 mT, and $T_0^{\parallel}$ = 18.7 mT for the same current amplitude. We

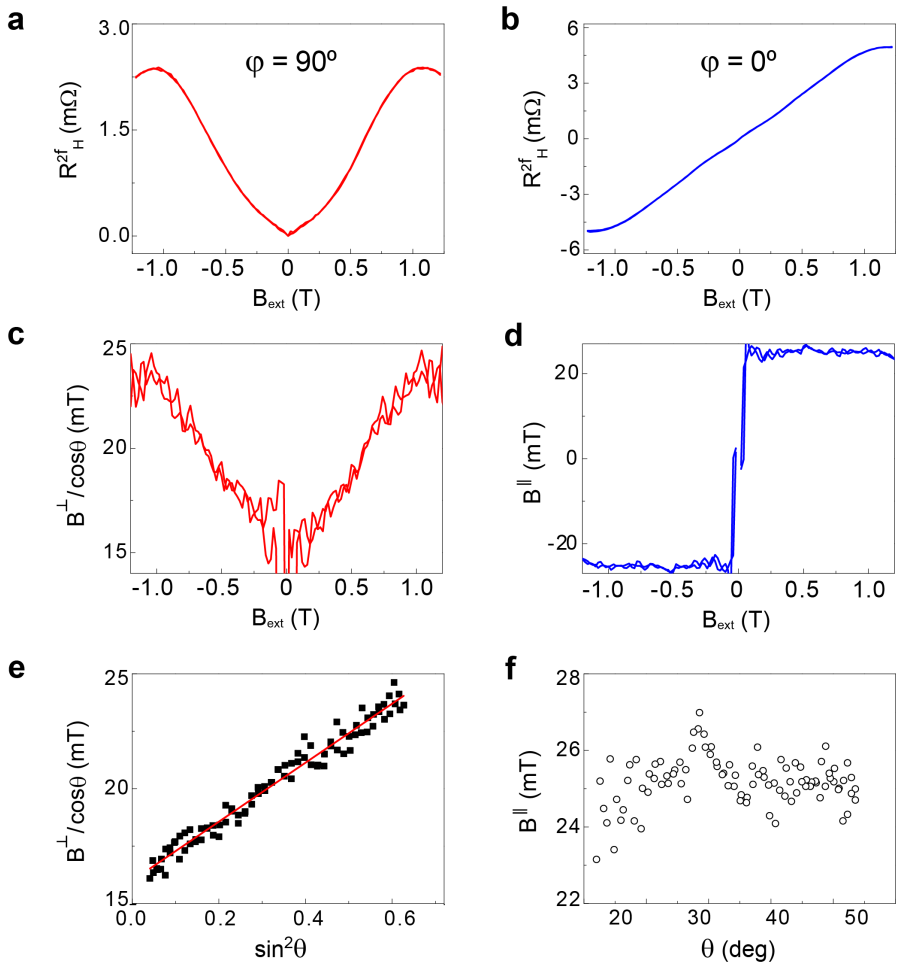

Figure S8. Second harmonic Hall resistance and current-induced spin-orbit fields measured on a 1000 x 500 nm^2 device. a, R_H^{2f} as a function of B_{ext} applied at $\theta_B = 82°$, $\varphi = 90°$ and **b,** $\theta_B = 82°$, $\varphi = 0°$. The amplitude of the ac current is 1.136 mA. **c,** Effective field $B^{\perp}/\cos\theta$ as a function of B_{ext} ($\varphi = 90°$). **d,** Effective field $B^{//}$ as a function of B_{ext} ($\varphi = 0°$). **e,** $B^{\perp}/\cos\theta$ as a function of $\sin^2\theta$ measured at $\varphi = 90°$. The solid line is a fit to the function $T_0^{\perp} + T_2^{\perp}\sin^2\theta$ with $T_0^{\perp}$ = -16.0 mT and $T_2^{\perp}$ = -12.8 mT. **f,** $B^{//}$ as a function of θ measured at $\varphi = 90°$.

attribute this effect to the larger current density flowing in the magnetic region of the 1000 x 500 nm^2 device due to the reduced width of the voltage probes.

S9. Measurements in the case of nonuniform magnetization

Our measurements are based on detecting small current-induced oscillations of the magnetization about its equilibrium direction, which is determined by the anisotropy field and $\mathbf{B}_{ext}$. The magnetization curves (R_H^f) measured for $\theta_B \leq 85°$ show reversible behavior beyond the switching field, consistently with coherent rotation of the magnetization towards $\mathbf{B}_{ext}$. At

$\theta_B > 85°$, however, we observe irreversible jumps of the Hall resistance due to the formation of magnetic domains. These jumps are also detected in the R_H^{2f} curves, as shown in Fig. S9 for a geometry $\theta_B = 87°$, $\varphi = 90°$ and $I = 635$ μA. For this reason, the measurements reported in this paper are limited to $\theta_B \leq 85°$.

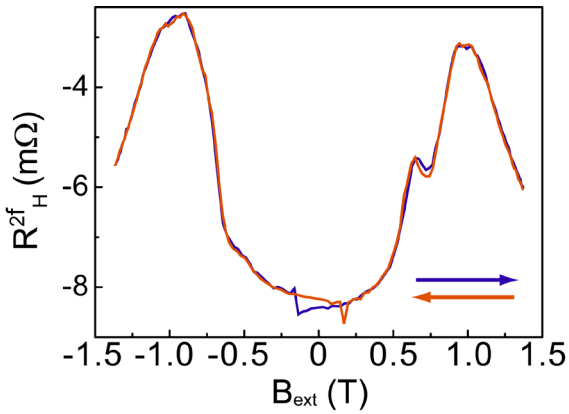

Figure S9. Second harmonic Hall resistance in the presence of magnetic domain nucleation. a, R_H^{2f} as a function of B_{ext} applied at $\theta_B = 87°$, $\varphi = 90°$. The amplitude of the ac current is 635 mA. A jump of the signal is observed between 0.5 and 1 T.

S10. Comparison of AC and DC detection methods

We present here a comparison of our AC detection method with DC measurements of the Hall voltage, analogue to those performed by Liu et al. in Refs. 5 and 6. These authors considered a scalar model where the torques due to the external field, magnetic anisotropy, and current are collinear. In the macrospin approximation, this leads to the following torque equation at equilibrium:

$$B_{ext}\sin(\theta_0 - \theta_H) - B_k \sin\theta_0 \cos\theta_0 + T(I) = 0. \qquad (50)$$

By estimating the equilibrium magnetization angle θ_0 using the AHE (Eq. 38), one can define two magnetic field values, $B_+(\theta_0)$ and $B_-(\theta_0)$, as the value of B_{ext} required to produce a given value of θ_0 for positive and negative current, respectively.[5] From Eq. 50 one has $B_\pm(\theta_0) = [B_k \sin\theta_0 \cos\theta_0 \mp T(|I|)]/\sin(\theta_0 - \theta_H)$ and, finally,

$$T(I) = \frac{B_-(\theta_0) - B_+(\theta_0)}{2}\sin(\theta_0 - \theta_H). \qquad (51)$$

In practice, $B_\pm(\theta_0)$ are calculated by measuring the Hall resistances for positive and negative current $[R_H(I_\pm)]$ as a function of applied field.

By assuming the simplest form for the torques, $\boldsymbol{T}^{\parallel} = T_0^{\parallel}\, \boldsymbol{m} \times (\boldsymbol{y} \times \boldsymbol{m})$ and $\boldsymbol{T}^{\perp} = T_0^{\perp}(\boldsymbol{y} \times \boldsymbol{m})$, Liu et al. used Eq. 51 to measure $T_0^{\parallel}$ and $T_0^{\perp}$ for B_{ext}applied in the *xz* and *yz* plane, respectively (note that, with respect to our notation, the *x* and *y* axis are interchanged in Refs. 5 and 6). For AlO_x/Co(0.6 nm)/Pt(2 nm) annealed in vacuum at 350 C, Liu et al. concluded that $T_0^{\parallel}$ = 0.33±0.06 mT/mA (1.7 mT per 10^7 A/cm^2) and that $T_0^{\perp}$= 0, within the sensitivity of the experiment (1.3 mT per 10^7 A/cm^2). Because the SOT amplitudes are generally very sensitive to the sample growth details, it is not surprising that we obtain different torque values, at least for $T_0^{\parallel}$. However, Eq. 51 assumes that the magnetization remains confined in the plane defined by the external field and *z* axis, which is not true if both $\boldsymbol{T}^{\parallel}$ and $\boldsymbol{T}^{\perp}$ are present, as can be seen from Eqs. 18, 19 and 24, 25 (see also Fig. 11b). Moreover, if the magnetization deviates from the *xz*

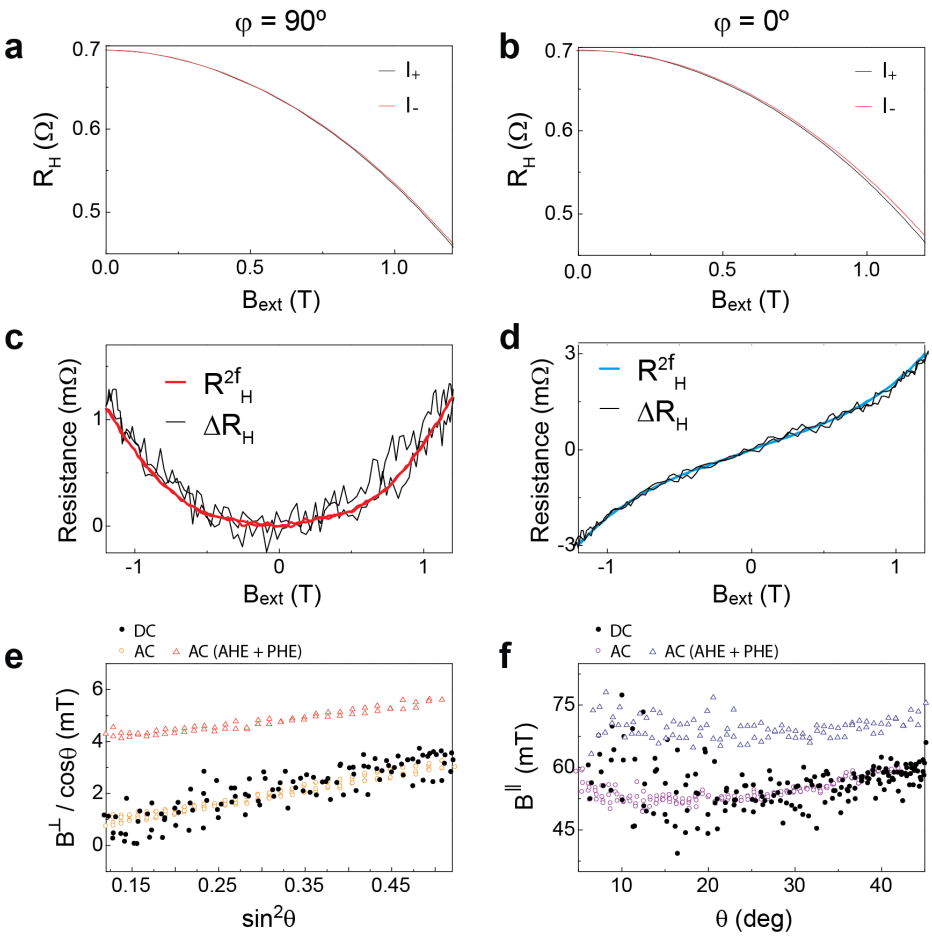

Figure S10. Comparison between AC and DC detection methods. R_H measured on a Hall cross of 3000 nm (current injection) by 500 nm (Hall voltage) for $I_{\pm}$= ±1.2 mA, θ_B = 86º, and **a,** φ = 90º, **b,** φ = 0º. **c, d,** Comparison of R_H^{2f} and $\Delta R_H/2$. **e,** Comparison of $B^{\perp}$ extracted from R_H^{2f} (open symbols) and ΔR_H (filled symbols). **f,** Same for $B^{\parallel}$. The data corrected for the PHE are also shown. The integration time used in the AC method was 10s. In the DC method, each field point has been averaged for 10 s.

or the *yz* plane, the PHE contributes to R_H in a way that is not symmetric for positive and negative current. These effects, as well as the presence of additional torque components besides $T_0^{\parallel}$ and $T_0^{\perp}$, have not been taken into account in the analysis of Refs. 5 and 6.

Here, we show that, if the PHE is neglected, the two methods give equivalent results, but that the AC measurements give a better signal-to-noise ratio compared to DC, as expected. Figures S10a and b show $R_H(I_+)$ and $R_H(I_-)$ measured for B_{ext}applied in the *yz* ($\varphi = 90°$) and *xz* ($\varphi = 0°$) plane, respectively. In Fig. S10c and d we compare R_H^{2f} with the corresponding quantity in a DC measurement, $\Delta R_H/2 = [R_H(I_+) - R_H(I_-)]/2$. The fields $B_+(\theta_0)$ and $B_-(\theta_0)$ introduced above can be easily derived from ΔR_H. We observe that, apart from the noise level, R_H^{2f} and ΔR_H present the same dependence on the external field. Figures S10e and f show that, if R_{PHE} is set to zero, the current-induced fields $B^{\perp}$ and $B^{\parallel}$ obtained from the analysis of R_H^{2f} and ΔR_H using Eqs. 40 and 41 give similar results, although the scattering of the DC data is much larger. The AC data corrected for the PHE are also shown. Clearly, the AC method allows for more sensitive measurements and, therefore, to work in a low current regime where the magnetization behaves coherently and thermal effects are small.

S11. Dynamic simulations of the m_y component generated by $T^{\parallel}$

As mentioned above and in the main text, a remarkable difference between our data and those reported by Liu et al. is the null result obtained for $\boldsymbol{T}^{\perp}$ in Ref. 5. We pointed out the reduced sensitivity of DC measurements and differences in sample preparation as possible clues for such a discrepancy. On the other hand, Liu et al. confuted the interpretation of previous measurements of $\boldsymbol{T}^{\perp}$ by noting that the spin transfer torque $\boldsymbol{T}^{\parallel}$ due to the spin Hall effect may induced a tilt of the magnetization along the *y* axis, similar to that expected by $\boldsymbol{T}^{\perp}$ (Ref. 5). This would be the case if $|T_0^{\parallel}| > B_k/2$, that is, if $T_0^{\parallel}$ is so large as to overcome the anisotropy field and induce switching. However, the method presented in this work is based on small oscillations of the magnetization and the torque amplitudes have been measured in the low current regime (Fig. 4 main text), which is very far from the regime $|T_0^{\parallel}| > B_k/2$ hypothized in Ref. 5. We have carried out dynamic simulations of the *x*, *y*, *z* magnetization components subject to either $\boldsymbol{T}^{\perp}+\boldsymbol{T}^{\parallel}$ or $\boldsymbol{T}^{\parallel}$ alone to confirm this point, by numerically solving the LLG equation $\dot{\boldsymbol{m}} = -|\gamma_0|[\boldsymbol{m} \times (\boldsymbol{B}_{ext} + \boldsymbol{B}_k) + \boldsymbol{T}^{\parallel} + \boldsymbol{T}^{\perp}] + \alpha\, \boldsymbol{m} \times \dot{\boldsymbol{m}}$, where γ_0 is the gyromagnetic ratio and α the Gilbert damping. The simulations were performed using the following parameters: B_k= 1 T, α =0.5, and

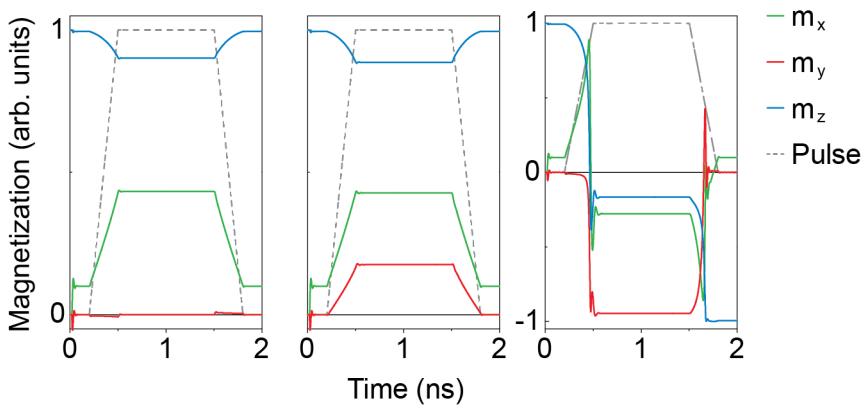

Figure S11. Dynamic simulations of m_x, m_y, and m_z for different torque amplitudes. a, $T_0^{\perp} = T_2^{\perp} = 0$ and $T_0^{\parallel}$ = 0.3 T, **b,** or $T_0^{\perp} = T_2^{\perp} = 0.15$ T and $T_0^{\parallel}$ = 0.3 T **c,** $T_0^{\perp} = T_2^{\perp} = 0$ and $T_0^{\parallel}$ = 0.6 T. The dashed line represents the injected current.

B_{ext}= 0.1 T, φ=0º, θ_H=90º. Figure S11a shows that for $T_0^{\perp} = T_2^{\perp} = 0$ and $T_0^{\parallel}$ = 0.3 T $< B_k/2$, no magnetization component appears along the y axis. A nonzero m_y only appears if $\boldsymbol{T}^{\perp}$ is turned on, as in Fig. S11b or when $T_0^{\parallel}$ = 0.6 T $> B_k/2$, as in Fig. S11c.

S12. Influence of thermal effects

It is well known that heating reduces the magnetic anisotropy field and saturation magnetization of thin films. Therefore ohmic heating induced by the current effectively softens the magnetization of the ferromagnetic layer, increasing the susceptibility of the magnetization to the spin torques. A consequence of this effect is to introduce a spurious increase of the torque amplitudes measured at high current, which may add itself to the intrinsic temperature dependence of the torques. However, heating effects are proportional to I^2 and hence should appear as an odd harmonic component of the Hall resistance, R_H^{3f}, whereas R_H^{2f} should reflect the presence of spin torque components that are linear with the current. To check the validity of this statement, we implemented Joule heating in our macrospin simulations and compared them with experimental data obtained for two different current amplitudes (Fig. S12). Heating was modeled by considering a reduced anisotropy field $B_k(1 - a_k I^2)$ and saturation magnetization $M_s(1 - a_M I^2)$, using the following parameters: B_k = 1 T, $\mu_0 M_s$ = 1 T, R_{AHE}= 0.8 Ω, R_{PHE}= 0.1 Ω, $T_0^{\perp}$ = -0.12 T, $T_2^{\perp}$ = -0.11 T, and $T_0^{\parallel}$ = 0.19 T. The coefficients a_k=0.14 and a_M=0.035 were derived from the measured current dependence of B_k and R_{AHE}, respectively. We performed simulations of R_H^f, R_H^{2f}, and R_H^{3f}, as shown in Fig. S12. In the top panels, we observe

a small decrease of the R_H^f amplitude at remanence, due to the decrease of M_s, and at high field due to the reduction of B_k. Both the experiments and simulations show a clear R_H^{3f} signal (bottom panels) that disappears when heating is turned off in the simulations (blue line). On the other hand, the measurements of R_H^{2f} normalized by the current amplitude nearly superpose (middle panels), meaning that heating effects have only a minor influence on the spin torque measurements in this current regime. This is in agreement with the current dependence of the torque coefficients reported in Fig. 4 of the main text, which is linear below j = 1.5 x 10^7 A/cm^2. Above this limit, our simulations show that R_H^{2f} gradually increases due to the reduction of M_s, whereas R_H^{3f} is affected by M_s (hysteretic part) and B_k (high-field part). Finally, we simulated the case where $\boldsymbol{T}^{\perp}$ is set to zero to check whether a heat-induced modulation of the anisotropy field can mimic the action of the field-like torque, as suggested in Ref. 5. This turns out not to be the case, since R_H^{2f} is zero in such a case (green line).

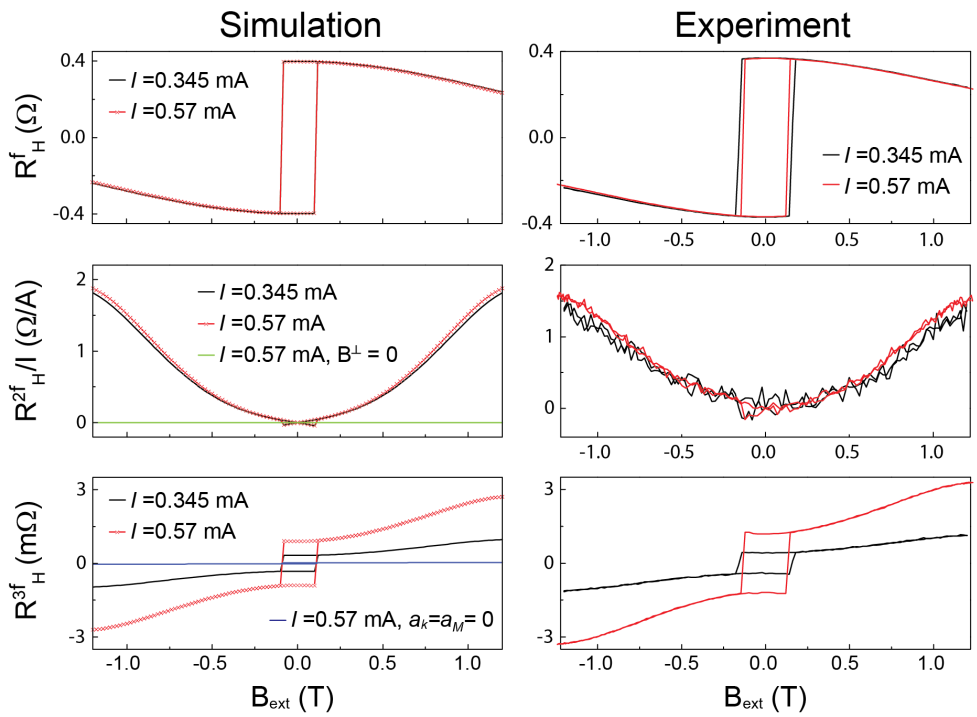

Figure S12. Macrospin simulations of thermal induced effects and comparison with experimental data. Simulations (left column) and measurements (right column) of R_H^f, R_H^{2f}, and R_H^{3f} for φ = 90º. The measurements were performed on a 1000 x 1000 nm^2 AlO_x/Co/Pt device. See text for details.

S13. Supplementary references

[1] Pauyac, C. O.,Wang, X., Chshiev, M. & Manchon, A. Angular dependence and symmetry of Rashba spin torque in ferromagnetic heterostructures, *http://arxiv.org/pdf/1304.4823*.

[2] Lindberg, O. Hall Effect. *Proc. Inst. Radio Engrs*. **40**, 1414-1419 (1952).

[3] Seki, T. et al., Giant spin Hall effect in perpendicularly spin-polarized FePt/Au devices, *Nat. Mater*. **7**, 125-129 (2008).

[4] Ibrahim, I. S., Schweigert, V. A. & Peeters, F. M. Diffusive transport in a Hall junction with a microinhomogeneous magnetic field. *Phys. Rev. B* **57**, 15416-15427 (1998).

[5] Liu, L., Lee, O. J., Gudmundsen, T. J., Ralph, D. C. & Buhrman, R. A. Current-Induced Switching of Perpendicularly Magnetized Magnetic Layers Using Spin Torque from the Spin Hall Effect. *Phys. Rev. Lett.* **109**, 096602 (2012).

[6] Liu, L., Pai, C. F., Li, Y., Tseng, H. W., Ralph, D. C. & Buhrman, R. A. Spin-torque switching with the giant spin Hall effect of tantalum. *Science* **336**, 555-558 (2012).